catalysts

MDPI

Article

Metal-Free Enhanced Photocatalytic Activation of Dioxygen by g-C_3N_4 Doped with Abundant Oxygen-Containing Functional Groups for Selective N-Deethylation of Rhodamine B

Jia Huang [1,*], Gang Nie [1] and Yaobin Ding [2,*]

[1] School of Resources and Environmental Sciences, Wuhan University, Wuhan 430079, China; niegangsteven@foxmail.com

[2] College of Resources and Environmental Science, South-Central University for Nationalities, Wuhan 430079, China

* Correspondence: jiahuang@whu.edu.cn (J.H.); yaobinding@mail.scuec.edu.cn (Y.D.)

Received: 25 October 2019; Accepted: 11 December 2019; Published: 18 December 2019

Abstract: To develop highly efficient heterogeneous photocatalysts for the activation of dissolved oxygen is very interesting in the field of green degradation of organic pollutants. In the paper, oxygen atom doped g-C_3N_4 (O-g-C_3N_4) was prepared via a facile chemical oxidation of g-C_3N_4 by peroxymonosulfate. X-ray photoelectron spectroscopy analysis suggests the oxidative treatment of g-C_3N_4 by peroxymonosulfate eVidently increased atomic percentage of oxygen on O-g-C_3N_4 surface to 6.9% as compared with 1.8% for g-C_3N_4. Meanwhile, the doped oxygen atom mainly existed as carbonyl and carboxyl groups. Optical characterization indicates the introduction of oxygen improved the response of O-g-C_3N_4 to visible light, and more obviously, separation of photo-generated h^+-e^-. 4-chloro-7-nitrobenzo-2-oxa-1,3-diazole (NBD-Cl) probe measurement indicates the formation of $O_2^{\bullet-}$ was dramatically enhanced through activation of dioxygen by photo-generated electrons in the O-g-C_3N_4 photocatalytic system. Through high performance liquid chromatography (HPLC) and Liquid chromatography–mass spectrometry (LC-MS) analysis, it was found rhodamine B (RhB) photocatalytic degradation by O-g-C_3N_4 followed step by step N-deethylation reaction pathways induced by the formed $O_2^{\bullet-}$, rather than the non-selective decomposition of the chromophore in RhB by other radicals, such as hydroxyl radicals. This study provides a facile method to develop oxygen atom doped g-C_3N_4 photocatalyst, and also clarifies its photocatalytic activation mechanism of molecular oxygen for N-deethylation reaction of RhB.

Keywords: photocatalysis; oxygen doped g-C_3N_4; activation of dioxygen; superoxide radicals; selective N-deethylation of rhodamine B

1. Introduction

Photocatalysis is a promising method, due to its potential to use solar light to generate reactive species, having a bright prospect in environment and energy fields [1,2]. Among them, graphitic carbon nitride (g-C_3N_4) has attracted much attention as a metal-free semiconductor, due to its excellent response to visible light, tunable electronic structure and promising application for decontamination, hydrogen eVolution and organic syntheses [3–8]. However, g-C_3N_4 photocatalysis usually exhibited unsatisfactory photocatalytic activity, due to the weak visible light absorption and high recombination of photo-generated carriers (h^+-e^-). To promote its photocatalytic performance, several measures have been carried out as fellows. (1) doping of g-C_3N_4 with nonmetal elements, such as carbon [9], O [10], P [11], S [12], B [13], N vacancy [14,15], and metal elements (Fe [16], Cu [17]); (2) improving the

separation of photo-generated h^+-e^- by preparation of thin- and single-layer g-C_3N_4 nanosheets [18], and (3) developing composite photocatalysts with other conductors or semiconductors (Ag [19], TiO_2 [20,21], WO_3 [22], BiOBr [23], Ag_3PO_4 [24]).

Oxygen doping was found to be an excellent strategy to promote the photocatalytic activity of g-C_3N_4. Li et al. introduced oxygen heteroatom in C_3N_4 by facile H_2O_2 hydrothermal approach at 140 °C for 10 h [8]. Guo and his coworkers fabricated holey structured g-C_3N_4 doped with edge oxygen via photo-Fenton reaction [25]. In these works, the photocatalytic activity of g-C_3N_4 was improved, due to the O-doping [10,25–27]. However, it was attributed to the enlarged surface area, extended visible light absorption, and improved separation of h^+-e^- of photocatalytic g-C_3N_4, eVen without normalizing for their specific surface areas. Therefore, the real contribution of separation of photo-generated h^+-e^- to the overall photocatalytic performance of g-C_3N_4 can hardly be eValuated. Moreover, the influence of oxygen doping on the formation of reactive radicals from photocatalytic g-C_3N_4 was not systematically investigated.

Therefore, we developed a facile method to dope g-C_3N_4 with oxygen by oxidation of g-C_3N_4 nanosheets with peroxymonosulfate (PMS) under ultrasonic treatment at 60 °C for 30 min. PMS is a commonly used strong oxidant with the redox potential of 1.82 V, higher than that of H_2O_2 (1.77 V) [28]. Moreover, PMS can be activated to produce sulfate and hydroxyl radicals with a higher oxidation potential of 2.5–3.1 V and 1.8–2.7 V [29]. Therefore, we infer that PMS can directly oxidize and indirectly oxidize g-C_3N_4 by the generated radicals, and oxygen atoms can be introduced into g-C_3N_4. After characterization by various physical-chemical methods, oxygen doped g-C_3N_4 (O-g-C_3N_4) nanosheets were successfully prepared. In comparison with g-C_3N_4, O-g-C_3N_4 nanosheets displayed extended absorption to visible light and much lower recombination of photo-generated h^+-e^-, which survived more photo-generated electrons for enhanced activation of dioxygen via one-electron reduction process. $O_2^{\bullet-}$ was confirmed as the dominant oxidant and induced step by step N-deethylation reaction of RhB in the O-g-C_3N_4 photocatalytic system. The reaction mechanism for RhB degradation is greatly different from the non-selective decomposition of the chromophore in RhB by other radicals, such as hydroxyl radicals reported in the previous literature. The selectivity of the end product of N-deethylation reaction of RhB rhodamine 110 was calculated as 75% in 75 min in the O-g-C_3N_4 photocatalytic system.

2. Results and Discussion

2.1. Characterization

Figure 1 presented the X-ray diffraction (XRD) of g-C_3N_4 and O-g-C_3N_4. Both samples displayed a sharp diffraction peak of (002) at 2θ = 27.4° and a weak peak of (100) at 2θ = 12.9°, indicating that oxygen doping has not changed the intrinsic crystal structure of g-C_3N_4.

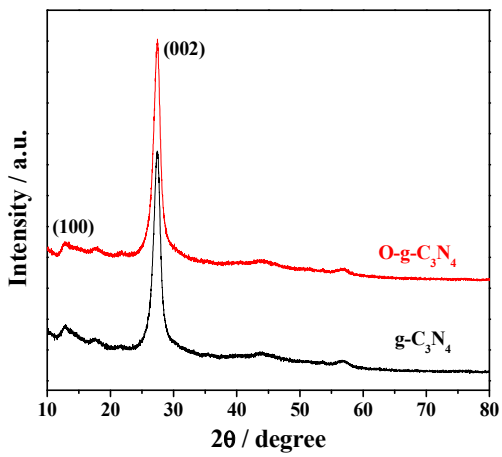

Figure 1. XRD patterns of g-C_3N_4 and O-g-C_3N_4.

The morphology of O-g-C_3N_4 photocatalysts was observed by Scanning electron microscopy (SEM) and transmission electron microscopy (TEM). Both samples displayed the characteristic morphologies of g-C_3N_4. As shown in Figure 2a,b, g-C_3N_4 and O-g-C_3N_4 photocatalysts were of highly condense two-dimensional sheets. However, it is difficult to quantify the nanosheet size of O-g-C_3N_4 and g-C_3N_4 to differentiate which one is smaller. The obvious change for O-g-C_3N_4 after oxygen doping was the presence of much more hole structure on the surface of O-g-C_3N_4 as observed in the TEM image in Figure 2d. The formation of a hole in O-g-C_3N_4 sample may be induced by the oxidative etch of the g-C_3N_4 surface by PMS, due to its high oxidation potential and higher oxidation ability of the generated sulfate and hydroxyl radicals. The similar observation was also reported in the oxidative treatment of g-C_3N_4 by photo-Fenton reaction [25] and by H_2O_2 in the hydrothermal process [16].

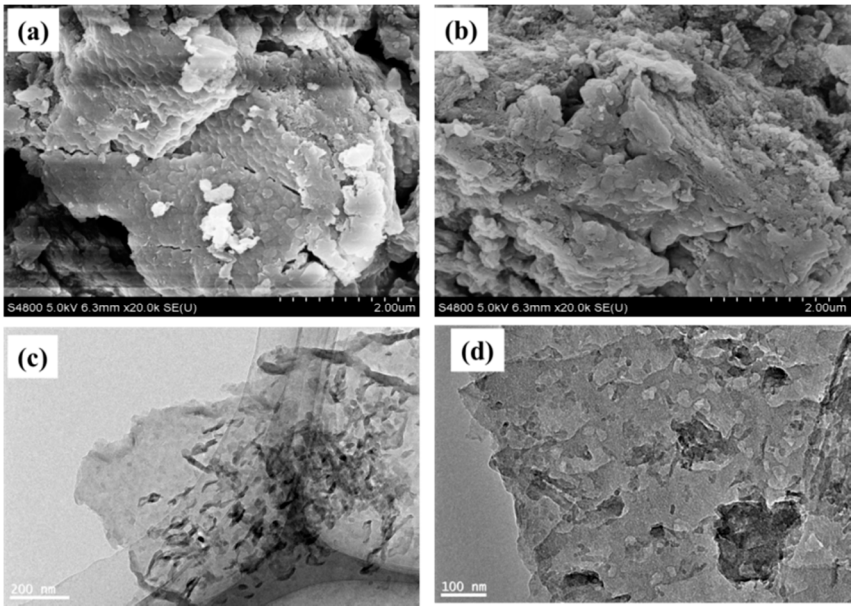

Figure 2. (**a**,**b**) SEM and (**c**,**d**) TEM images of (**a**,**c**) g-C_3N_4 and (**b**,**d**) O-g-C_3N_4.

The effect of PMS oxidation on specific surface area (SSA) of O-g-C_3N_4 photocatalysts was investigated through BET analysis. As seen in Figure 3, the SSA of g-C_3N_4 was 14.5 m^2/g, and was changed to 14.7 m^2/g after the doping of oxygen. The result indicates that the oxidation treatment by PMS only tuned the surface oxygen groups on O-g-C_3N_4 photocatalysts, rather than the greatly-changed surface area of bulk C_3N_4 photocatalysts, as observed in the chemical and thermal exfoliation of bulk g-C_3N_4 into single or few layers g-C_3N_4 nanosheets [30,31].

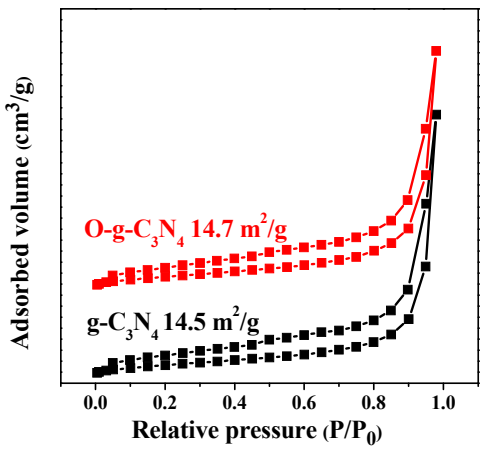

Figure 3. N_2 adsorption-desorption isotherms of g-C_3N_4 and O-g-C_3N_4 samples.

Energy Dispersive X-Ray Spectroscopy (EDS) and X-ray photoelectron spectroscopy (XPS) were used to measure the percentages of doped oxygen in O-g-C_3N_4 photocatalysts. Firstly, both EDS and XPS analysis indicated that g-C_3N_4 and O-g-C_3N_4 photocatalysts contained C, N and O elements (Figure 4a, Figures S1 and S2). As shown in Figures S1 and S2 (Supplementary Materials), EDS analysis presented that the atomic percentage of oxygen in O-g-C_3N_4 sample was 3.16%, a little higher than that (2.73%) in the g-C_3N_4 sample. The more obvious change for oxygen doping was observed on the surface of O-g-C_3N_4 sample as characterized by XPS. Through XPS analysis, the atomic percentage of O elements was measured as 1.8% for g-C_3N_4 photocatalyst. After treatment by PMS, the value was increased to 6.9% by 2.83 times for O-g-C_3N_4 photocatalyst (Figure 4a). These results indicated that oxidative treatment by PMS tended to tune the surface oxygen amount because the oxidation reaction induced by PMS mainly processed on the surface of g-C_3N_4 samples. To better reveal the chemical state of C, N and O in the two photocatalysts, the XPS of C1s, N1s and O1s were also analyzed. The C1s spectra in Figure 4b represented sp^2-bonded carbon at 287.5 eV was the main carbon species in the g-C_3N_4 [32]. However, the surface content of sp^2-bonded carbon in total carbon was much decreased from 84% for g-C_3N_4 to 51.2% for O-g-C_3N_4 sample. Accordingly, due to the oxidation effect by PMS treatment, the intensity of the peak of at O=C–O or C–O groups 288.1 eV was greatly increased to 31.6% for O-g-C_3N_4 sample. The result was further supported by the increased of oxygen groups on O-g-C_3N_4 surface (Figure 4c). The O1s spectra of the two samples can be mainly consist of two peaks of the carbonyl group (C=O) and carboxyl group (O=C–O) at 531.0 eV and 532.0 eV [33]. As clearly depicted in Figure 4c, the oxidation of g-C_3N_4 by PMS changed little the surface percentage of C=O and O=C–O groups, while much more obvious change was the enhanced intensity of O1s spectra of O-g-C_3N_4 sample than that of the g-C_3N_4 sample.

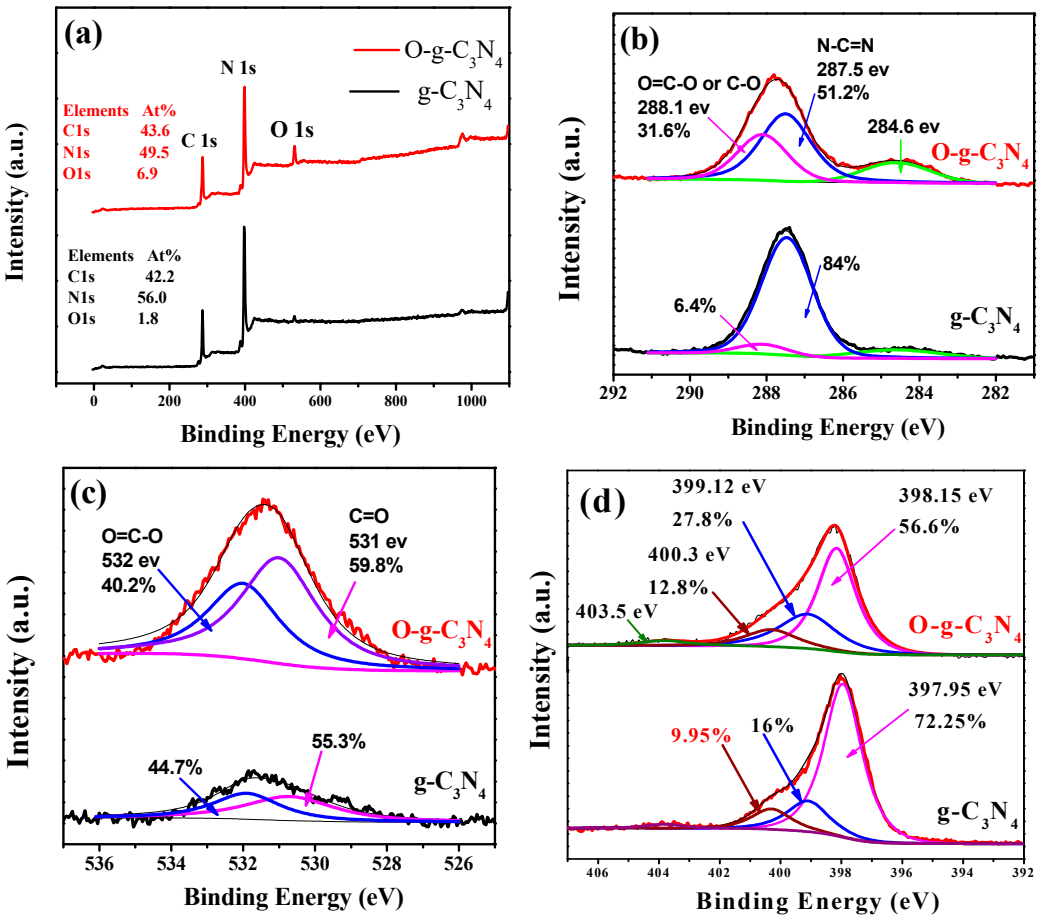

Figure 4. XPS spectrum of g-C_3N_4 and O-g-C_3N_4: (**a**) Wide survey, high-resolution XPS spectra of (**b**) C 1s, (**c**) O 1s and (**d**) N 1s.

As seen in Figure 4d, the N 1s spectrum was composed of three peaks of C–N=C (sp^2-hybridized nitrogen), N–C_3 (sp^3-hybridized nitrogen) and N–H group (amino functional groups with a hydrogen atom), respectively [34]. For the g-C_3N_4 sample, the peak of C–N=C group was located at 397.95 eV. After oxidation by PMS, the peak of C–N=C group shifted to 398.15 eV. The positive shift of binding energy was more likely, due to the doping of more oxygen atoms in the C_3N_4 skeleton as an electron-withdrawing group.

The UV-visible absorption of O-g-C_3N_4 samples was studied by diffuse reflective spectra (DRS). As depicted in Figure 5a, the absorption of O-g-C_3N_4 sample was all enhanced in the UV-visible spectrum from 200 nm to 600 nm, due to the doping of oxygen atoms. Accordingly, the color was changed from light yellow for the g-C_3N_4 sample to yellow for O-g-C_3N_4 sample (Figure S3). The enhance absorption effect was mainly attributed to the doping of more oxygen groups, such as carbonyl and carboxyl groups in O-g-C_3N_4 sample. Further, the band gap (E_g) was calculated by fitting with the Tauc/David–Mott model ($(\alpha h\nu)1/n = A(h\nu - E_g)$) [14,35]. As seen in Figure 5b, the E_g value was obtained as 2.79 and 2.82 eV for O-g-C_3N_4 and g-C_3N_4, respectively.

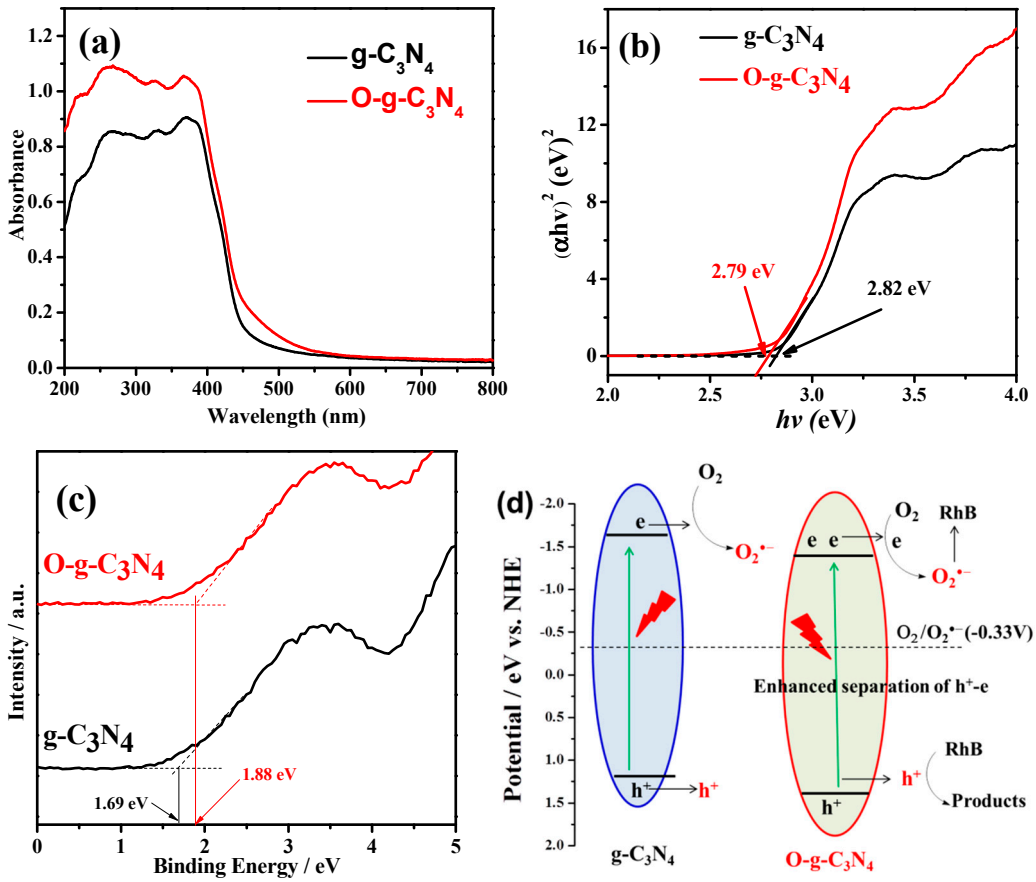

Figure 5. Optical properties of g-C_3N_4 and O-g-C_3N_4: (**a**) DRS spectra, (**b**) plots of $(\alpha h\nu)^{1/2} - h\nu$, (**c**) valence band (VB) XPS spectra and (**d**) scheme of VB and conduction band (CB) position.

To further gain band structures of both samples, the valence band (VB) maximum was measured by VB XPS measurement. As depicted in Figure 5c, the difference value of between the Fermi level (E_F) value and VB maximum value (ΔE) was about 1.69 and 1.88 eV for g-C_3N_4 and O-g-C_3N_4 samples, respectively. Consequently, the conduction band (CB) and VB positions of g-C_3N_4 and O-g-C_3N_4 could be obtained by using $E_{VB} = \Delta E - E_{vac} + W_s$ [36], where E_{vac} is a constant of 4.5 eV, and W_s is work functions. The W_s of g-C_3N_4 is 4.0 eV [36]. As seen in Figure 5b, the band gap of g-C_3N_4 and O-g-C_3N_4 was 2.79 and 2.82 eV. Therefore, the VB positions (vs. NHE) were determined to be 1.38 and 1.19 eV for

O-g-C_3N_4 and g-C_3N_4, respectively. Accordingly, the E_{CB} was calculated as −1.63 and −1.41 eV for O-g-C_3N_4 and g-C_3N_4 (Figure 5d and Table 1).

Table 1. Elemental composition, band structure and RhB degradation for g-C_3N_4 and O-g-C_3N_4.

Samples	Oxygen (at.%)	Surface Oxygen (at.%)	E_g (eV)	E_{VB} (eV)	E_{CB} (eV)	S_{BET} (m^2/g)	RhB Removal (%)	k (min^{-1})
g-C_3N_4	2.73	1.8	2.82	1.19	−1.63	14.5	55.9	0.0032
O-g-C_3N_4	3.16	6.9	2.79	1.38	−1.41	14.7	97.8	0.079

The high performance separation of photo-generated carriers is the key step to survive and form reactive species. Therefore, we used photoluminescence (PL) emission spectra and photocatalytic H_2 eVolution rate (HER) to study the separation of photo-generated carriers formed from photocatalytic g-C_3N_4 and O-g-C_3N_4 [37,38]. As clearly found in Figure 6a, an obviously lower PL intensity was observed with O-g-C_3N_4 than that with g-C_3N_4, demonstrating that the doping of oxygen greatly improved the separation of photo-generated h^+-e^-. Moreover, the dramatic enhancement of H_2 eVolution by photocatalytic O-g-C_3N_4 in comparison with photocatalytic g-C_3N_4 indicating much more photo-generated electrons survived, due to the doping of oxygen in the g-C_3N_4 photocatalyst (Figure 6b).

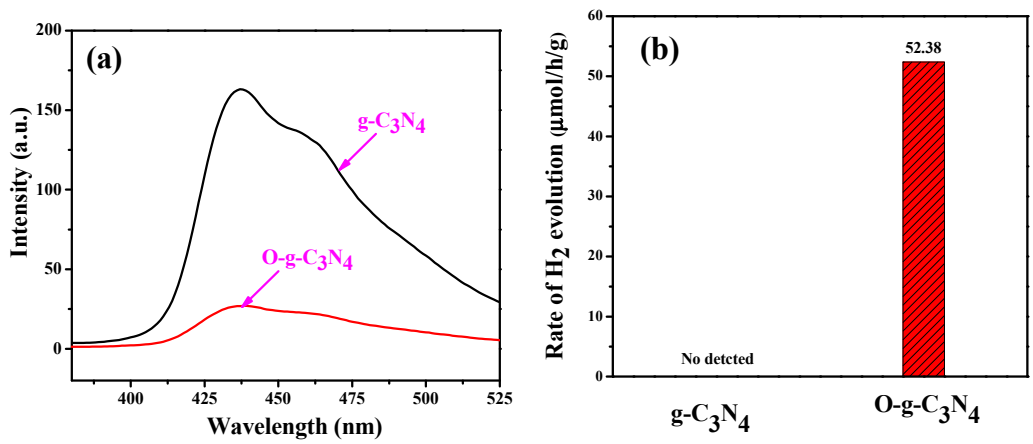

Figure 6. (**a**) Comparison of photoluminescence (PL) spectra and (**b**) photocatalytic H_2 eVolution rate of pure g-C_3N_4 and O-g-C_3N_4 samples.

Based on the characterization above, the oxidative treatment of g-C_3N_4 greatly increased oxygen content on the surface of O-g-C_3N_4. The surface atomic percentage of O1s elements was increased from 1.8% for g-C_3N_4 to 6.9% for O-g-C_3N_4 photocatalyst (Figure 4a). The doped oxygen atom mainly existed as acarbonyl group and carboxyl group (Figure 4c). The dope of oxygen in O-g-C_3N_4 improved the response to visible light (Figure 5a), and more importantly, promoted efficient separation of photo-generated h^+-e^- (Figure 6).

2.2. Photocatalytic Activity of O-g-C_3N_4 for Selective N-Deethylation of RhB

Firstly, the effect of oxidant PMS amount during the oxidative treatment process of g-C_3N_4 on the photocatalytic activity of O-g-C_3N_4 for RhB degradation was investigated. As Figure 7a, as the amount of added PMS was increased from 1 to 2 g, RhB degradation was increased from 54% to 100% in 60 min, as compared with 18% removal for g-C_3N_4 photocatalyst. Accordingly, the reaction rate constant k for RhB degradation was 0.0032 min^{-1} for g-C_3N_4, and increased by 4.4 and 24.7 times to 0.014 and 0.079 min^{-1} for O-g-C_3N_4-1 and O-g-C_3N_4-2, respectively. However, when PMS amount was increased further to 5 g, the RhB degradation in 60 min was reduced to 76%, and k value declined to 0.022 min^{-1} for O-g-C_3N_4-5. Moreover, Table S1 presented the comparison of the performance of

as-prepared O-g-C_3N_4 samples and other doped g-C_3N_4 previously reported for RhB degradation. As can be clearly seen, as-prepared O-g-C_3N_4 presented excellent photocatalytic performance among the reported doped g-C_3N_4 catalyst for RhB degradation and the highest enhancement effect than g-C_3N_4. Therefore, PMS amount was optimized as 2 g for the preparation of O-g-C_3N_4 samples, which were used as a model catalyst to study the enhanced photocatalytic mechanism of oxygen doping in the g-C_3N_4 photocatalyst.

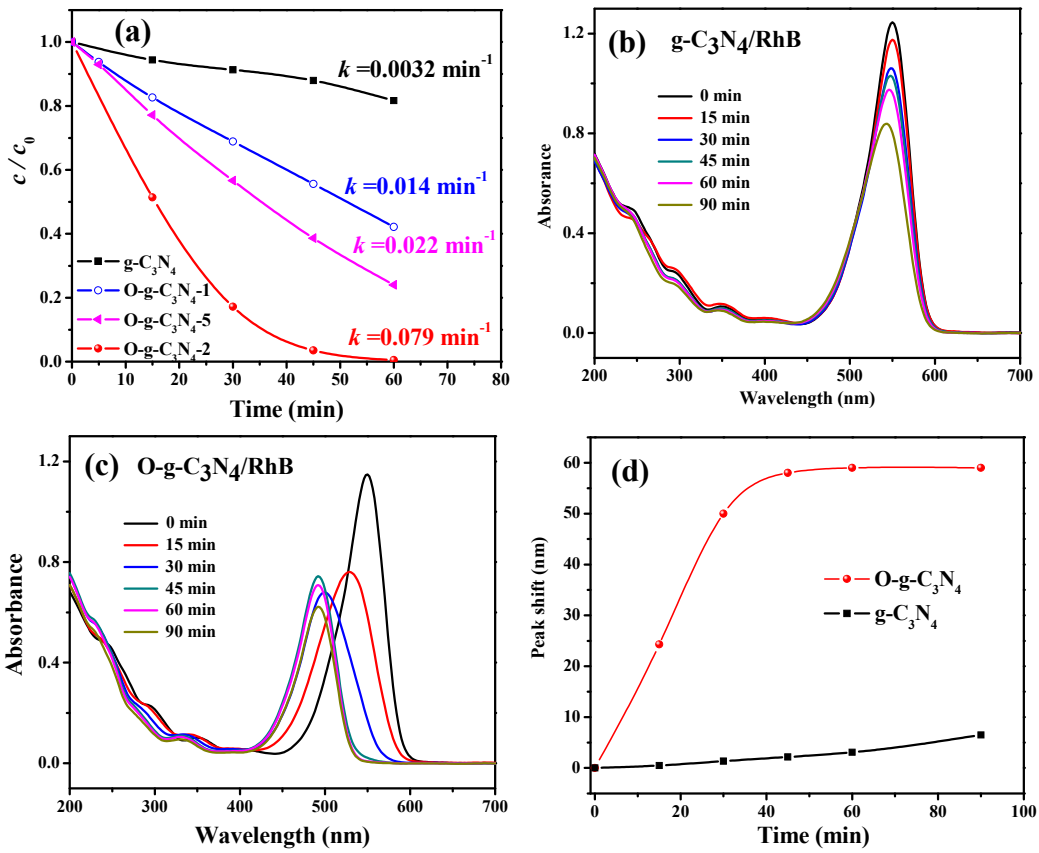

Figure 7. (**a**) Degradation profile of RhB calculated based on the absorption at 554 nm by photocatalytic g-C_3N_4 and O-g-C_3N_4 prepared with different PMS amounts. UV-vis absorption spectral changes for RhB degradation in the (**b**) g-C_3N_4 and (**c**) O-g-C_3N_4 photocatalytic systems. (**d**) Hypsochromic shifts of the maximum absorption wavelength for RhB degradation by photocatalytic g-C_3N_4 and O-g-C_3N_4.

To more clearly reveal the RhB degradation process, UV-visible absorption spectrum of the reaction solution in the photocatalytic system of g-C_3N_4 and O-g-C_3N_4 was recorded. As shown in Figure 7b, the initial RhB solution showed the maximum absorption wavelength of 553 nm. As the photocatalytic reaction proceeded, the maximum absorption of RhB at 553 nm slowly declined, suggesting that RhB was readily degraded by using g-C_3N_4 as a photocatalyst. After calculation based on the decrease of maximum absorption at 553 nm, about 18% RhB was decomposed in 60 min in the g-C_3N_4 photocatalytic system. Moreover, the maximum absorption wavelength shifted from 553 nm to 546 nm by 7 nm (Figure 7d). Comparably, the used of O-g-C_3N_4 as a photocatalyst induced the rapid decrease of maximum absorption of RhB at 553 nm. After 60 min reaction, the absorption of the reaction solution at 553 nm was decreased to zero, indicating that RhB was completely decomposed (Figure 7c). More obviously, the maximum absorption of the reaction solution wavelength shifted dramatically from 553 nm to 494 nm by 59 nm (Figure 7d). Based on the previous literature [39–42] and LC-MS analysis discussed below, the blue shift of the RhB reaction solution suggests that N-deethylation of rhodamine B was conducted. Therefore, the doping of oxygen atom in O-g-C_3N_4 eVidently enhanced the photocatalytic activity for the N-deethylation of RhB.

To further reveal the N-deethylation process of RhB by photocatalytic O-g-C_3N_4, the possible intermediates were analyzed by LC and LC-MS. Firstly, Figure 8a shows there are two main peaks occurred in the LC spectrum for RhB solution, suggesting that commercial RhB containing another impurity. The impurity was the chemical corresponding to the removal of one ethyl group from RhB (P1). Moreover, as the reaction proceeded, the peak area of RhB rapidly declined, suggesting the efficient degradation of RhB by photocatalytic O-g-C_3N_4. Meanwhile, new LC peaks appeared, indicating that intermediates were formed from RhB degradation by photocatalytic O-g-C_3N_4. These intermediates were identified by LC-MS. Five products were detected in the reaction solution besides RhB, and their main fragment ions and molecular structure were listed in Table 2. The detected products are generated from N-deethylation of RhB. As the reaction proceeded, the peak area of P1 firstly increased, and decreased after reaction for 15 min. The reaction time for the occurrence of the largest peak area of P1 and P2 was 15 min, while that of P3, P4, and P5 were prolonged to 30 min, 45 min and 75 min, indicating stepwise N-deethylation process of RhB → P1 → P2 → P3 → P4 → P5 in the O-g-C_3N_4 photocatalytic system (Scheme 1). The similar N-deethylation products of RhB were observed in several photocatalytic systems [40,43–45].

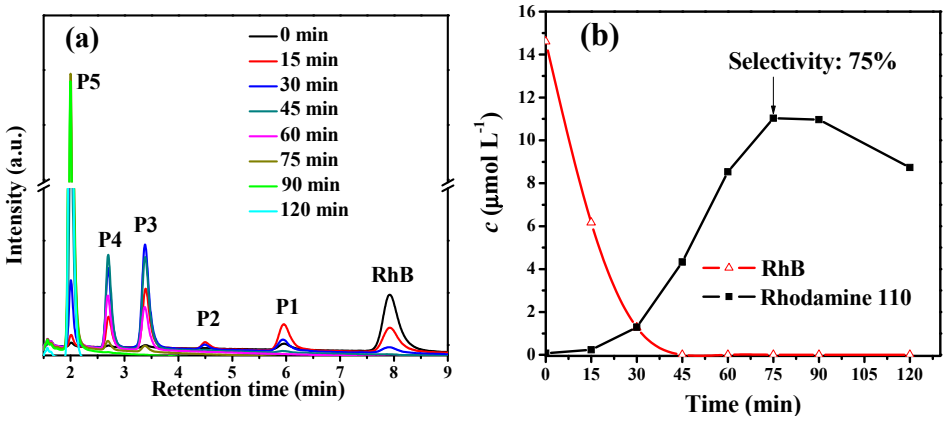

Figure 8. (**a**) HPLC spectra of degradation intermediated of RhB and (**b**) the profile for concentration of rhodamine 110 as a function of reaction time in the O-g-C_3N_4 photocatalytic system.

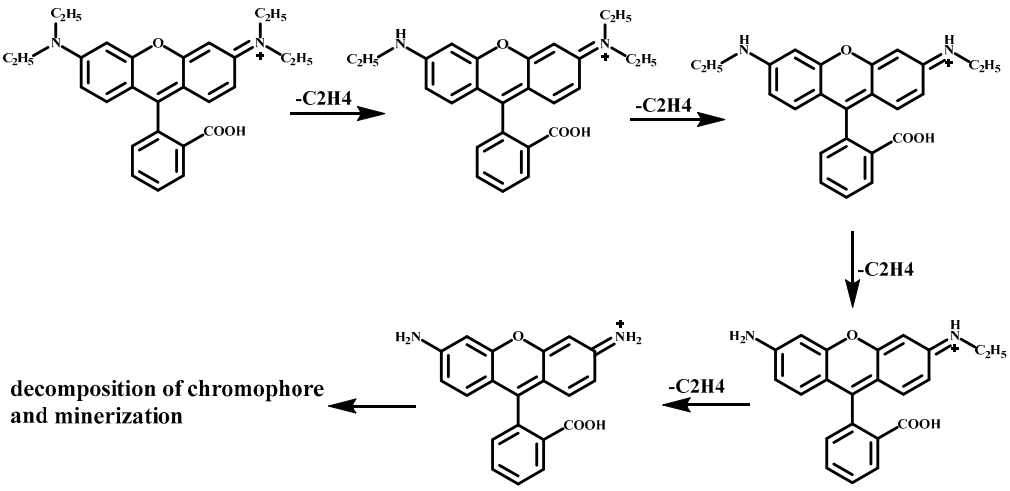

Scheme 1. Stepwise N-deethylation process of RhB in the O-g-C_3N_4 photocatalytic system.

Table 2. LC-MS information about main fragment ions of degradation intermediated of RhB in the O-g-C_3N_4 photocatalytic system by LC-MS (positive ion mode).

HPLC Peaks	Retention Time (min)	Corresponding Intermediates of RhB	ESI(-)MS2 m/z	Assigned Substrates
RhB	7.753	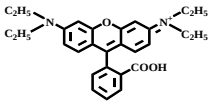	443.2 (100%) 444.2 (31.5%) 445.2 (5.4%)	$(RhB\text{-}Cl)^+$ $(RhB\text{-}Cl+H)^+$ $(RhB\text{-}Cl+2H)^+$
P1	6.157	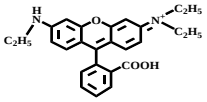	415.2 (100%) 416.2 (29.3%) 417.2 (4.8%)	$P1^+$ $(P1+H)^+$ $(P1+2H)^+$
P2	4.890	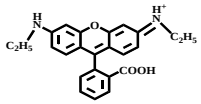	387.2 (100%) 388.2 (27.1%) 389.2 (4.1%)	$P2^+$ $(P2+H)^+$ $(P2+2H)^+$
P3	3.640	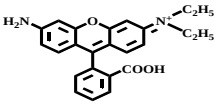	387.2 (100%) 388.2 (27.1%) 389.2 (4.1%)	$P3^+$ $(P3+H)^+$ $(P3+2H)^+$
P4	3.010	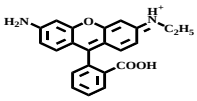	359.1 (100%) 360.1 (24.9%) 361.1 (3.6%)	$P4^+$ $(P4+H)^+$ $(P4+2H)^+$
P5	2.273	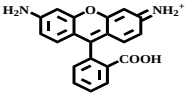	331.1 (100%) 332.1 (22.7%) 333.1 (3.1%)	$P5^+$ $(P5+H)^+$ $(P5+2H)^+$

To accurately eValuate the N-deethylation process of RhB, the concentration of generated P5 was measured in the reaction process by using a standard material of rhodamine 110. As depicted in Figure 8b, as the reaction preceded, the concentration of rhodamine 110 was gradually increased, and reached a maximum of 11.03 μmol/L in 75 min. Through calculation, the selectivity of rhodamine 110 was as high as 75% in 75 min. The value was consistent with the contribution of $O_2^{\bullet-}$ to degradation of RhB (74.5%) as seen in Figure 9c, suggesting stepwise N-deethylation process of RhB was mainly induced by the produced $O_2^{\bullet-}$ in the O-g-C_3N_4 photocatalytic system. When the reaction further proceeded, the concentration of rhodamine 110 declined, suggesting it can be further degraded by generated h^+ and $O_2^{\bullet-}$ in O-g-C_3N_4 photocatalytic system.

To fully understand N-deethylation process of RhB over O-g-C_3N_4 photocatalyst, the adsorption of RhB on O-g-C_3N_4 surface was eValuated with g-C_3N_4 as a comparison. As seen in Figure S4, the adsorption/desorption of RhB on catalyst surface can quickly reach equilibrium in 30 min. About 14.8% and 8.6% of RhB can be removed via the adsorption effect on the surface of g-C_3N_4 and O-g-C_3N_4 catalysts. The higher adsorption of RhB on O-g-C_3N_4 than that on g-C_3N_4 was attributable to the enhanced electrostatic interaction between RhB and O-g-C_3N_4, due to the more negatively charged surface of O-g-C_3N_4 at reaction pH of 5. As seen in Figure S5, O-g-C_3N_4 had an isoelectric point (pH_{pzc}) at 4.0, while pH_{pzc} of g-C_3N_4 was about 4.9. At reaction pH 5, the surface of O-g-C_3N_4 was more negative than that of g-C_3N_4, which facilitated the adsorption of cationic dye RhB on the surface of O-g-C_3N_4. As characterized by XPS in Figure 4c, the doped oxygen atomics existed in the form of carbonyl and carboxyl groups. At reaction pH 5, surface carboxyl groups can behave as a negatively charged adsorption sites to electrostatically link with the positive diethylamine groups in RhB (Figure S6). Under visible light irradiation, RhB degradation occurred preferentially via the stepwise N-deethylation attacked by formed $O_2^{\bullet-}$ in O-g-C_3N_4 photocatalytic system.

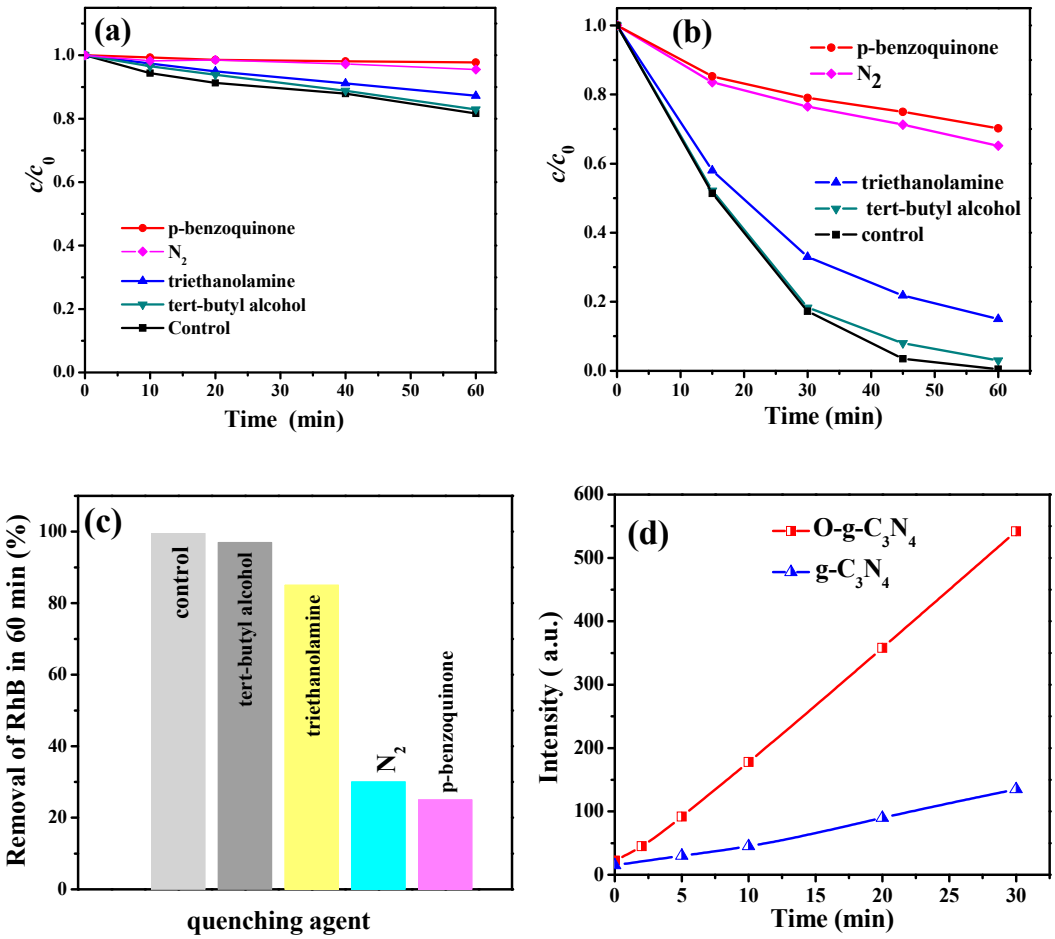

Figure 9. Effects of different quenchers on RhB degradation over (**a**) g-C_3N_4 and (**b**,**c**) O-g-C_3N_4 under visible light irradiation. (**d**) Measure the eVolution of $O_2^{\bullet-}$ radicals in the different systems by photoluminescence measurement.

2.3. Radicals Identification and Catalytic Mechanism

Previous literature indicate h^+, $O_2^{\bullet-}$ and ·OH were generally formed as free radical species from photocatalytic C_3N_4 for the decomposition of organic pollutants and transformation of toxic metallic contaminants. Therefore, the generation of the three reactive species was checked in O-g-C_3N_4 photocatalytic systems by using TBA, TEA and BQ as efficient quenching agents, respectively [46,47]. As clearly seen in Figure 9a, the addition of 25 mM BQ exhibited much inhibition to RhB degradation by photocatalytic g-C_3N_4 than other quenching agents, such as TEA and TBA, suggesting that $O_2^{\bullet-}$ was the dominant oxidant for RhB degradation over photocatalytic g-C_3N_4. Meanwhile, the continuous bubbling of N_2 also greatly depressed RhB degradation over photocatalytic g-C_3N_4, indicating the importance of dissolved oxygen as the precursor of $O_2^{\bullet-}$.

Similarly, as seen in Figure 9b,c, RhB degradation in the O-g-C_3N_4 photocatalytic system was greatly inhibited by the addition of 25 mM BQ. The RhB degradation rate in 60 min declined from 99.5% to 25% by about 74.5%, due to the presence of BQ. The result hinted the pivotal role of $O_2^{\bullet-}$ in RhB photocatalytic degradation by O-g-C_3N_4. Moreover, the addition of TEA decreased RhB degradation in 60 min to 85%, suggesting that photo-generated holes also made a contribution to RhB degradation by photocatalytic O-g-C_3N_4. Comparably, the addition of TBA showed little depress to RhB degradation, suggesting there are little ·OH was formed in the photocatalytic system. Finally, dissolved oxygen as the precursor of $O_2^{\bullet-}$ was also checked by the inlet of N_2. It was found that the introduction of N_2 showed comparable depress effect on RhB degradation as that by the addition of BQ. Therefore, it can be inferred that $O_2^{\bullet-}$ was produced from the activation of dioxygen in the reaction solution

by photo-generated electrons. In conclusion, $O_2^{\bullet-}$ was the major oxidant for RhB degradation by photocatalytic g-C_3N_4 and O-g-C_3N_4 with the minor role of photo-generated holes.

The conclusion was further supported by the enhanced generation of $O_2^{\bullet-}$ from photocatalytic O-g-C_3N_4 than that in the g-C_3N_4 photocatalytic system as observed in Figures 9d and 10. In the first set of experiments, NBD-Cl was used as the fluorescent probe to compare the formation of $O_2^{\bullet-}$ in the two systems [48]. Figure 9d displays the fluorescent intensity of the reaction product of $O_2^{\bullet-}$ and NBD-Cl in the O-g-C_3N_4 photocatalytic system was five times of that in the g-C_3N_4 photocatalytic system, indicating that dramatic promoting generation of $O_2^{\bullet-}$ over photocatalytic O-g-C_3N_4. Moreover, the enhanced formation of $O_2^{\bullet-}$ over photocatalytic O-g-C_3N_4 was also confirmed by electron spin resonance (ESR). In Figure 10, there were no obvious signals of $O_2^{\bullet-}$-5,5-dimethyl-1-pyrroline N-oxide (DMPO) adduct in the g-C_3N_4 photocatalytic system, while in the presence of O-g-C_3N_4 as a photocatalyst, the intensity of ESR signals of $O_2^{\bullet-}$-DMPO adduct was much bigger. Moreover, it was also found that the inlet of N_2 in the reaction solution decreased the intensity of ESR signals of $O_2^{\bullet-}$-DMPO adduct in the O-g-C_3N_4 photocatalytic system, further confirming dissolved oxygen as the precursor of $O_2^{\bullet-}$. Based on the discussion above, the dope of oxygen in O-g-C_3N_4 improved the phtocatalytic activity especially for dioxygen activation and the generation of $O_2^{\bullet-}$.

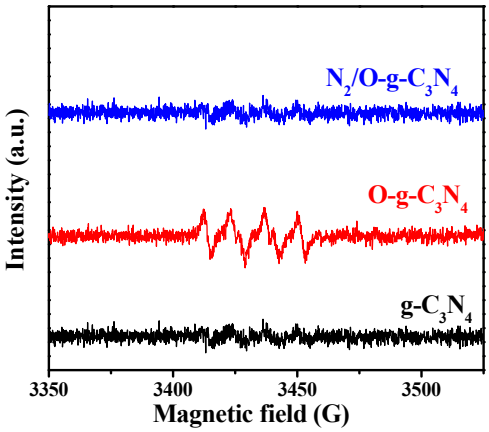

Figure 10. ESR spectra of superoxide radicals ($O_2^{\bullet-}$) spin-trapped by DMPO.

Based on the discussion above, the oxidative treatment of g-C_3N_4 greatly increased oxygen content on the surface of O-g-C_3N_4. The atomic percentage of O1s elements was increased from 1.8% for g-C_3N_4 to 6.9% for O-g-C_3N_4 photocatalyst. The doped oxygen atom mainly existed as a carbonyl group and carboxyl group. The dope of oxygen in O-g-C_3N_4 improved the response to visible light (Figure 5a), and more importantly, promoted efficient separation of photo-generated h^+-e^- (Figure 6), producing more reactive species. Especially, the formation of $O_2^{\bullet-}$ was dramatically enhanced in the O-g-C_3N_4 photocatalytic system, as seen in Figures 9d and 10. At reaction pH 5, negatively charged surface facilitated adsorption of RhB via electrostatic effect (Figure S6). Consequently, under visible light irradiation, RhB degradation processed preferentially via the stepwise N-deethylation attacked by formed $O_2^{\bullet-}$ in O-g-C_3N_4 photocatalytic system. The selective and stepwise N-deethylation reaction of RhB by photocatalytic O-g-C_3N_4 is quite different from the non-selective decomposition of the chromophore in RhB by other radicals, such as hydroxyl radicals. The selectivity of the end product of N-deethylation reaction of RhB rhodamine 110 was calculated as 75% in 75 min in the O-g-C_3N_4 photocatalytic system.

2.4. Stability of O-g-C_3N_4

Stability of O-g-C_3N_4 was eValuated by performing RhB degradation by recycled photocatalysts for several cycles. As shown in Figure 11, O-g-C_3N_4 presented excellent photocatalytic stability for RhB degradation as indicated by as high as 95% removal of RhB in the fifth run. In addition, O-g-C_3N_4

also exhibited high structure stability as confirmed by no obvious change of XRD characteristic peaks (Figure 11b).

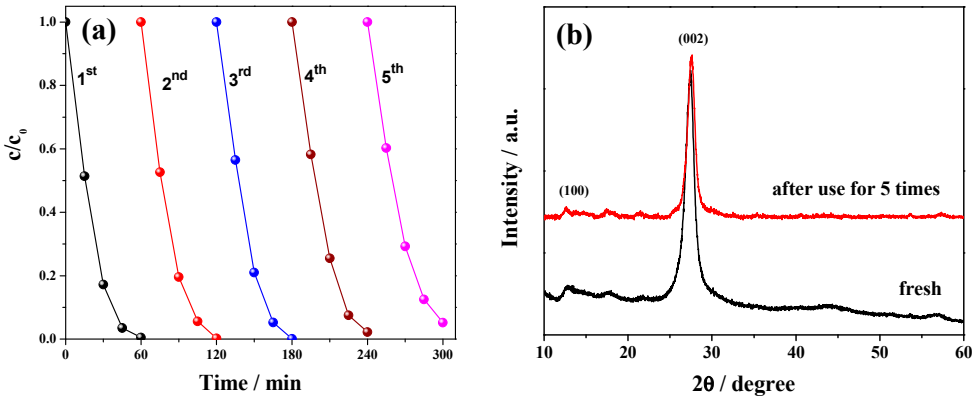

Figure 11. (**a**) Degradation profiles of RhB by recycled O-g-C_3N_4 for five times. (**b**) XRD of the fresh and used O-g-C_3N_4 for five times.

3. Materials, Experiment and Analysis Methods

3.1. Materials

Melamine, triethanolamine (TEA), peroxylmonosulfate (PMS), tert-butyl alcohol (TBA), 4-chloro-7-nitrobenzo-2-oxa-1,3-diazole (NBD-Cl), p-benzoquinone (BQ), rhodamine B (RhB) and rhodamine 110 chloride (CAS 13558-31-1) were obtained from Aladdin Biochemical Technology Co., Ltd., Shanghai, China. All the used reagents were analytic reagent grade.

3.2. Preparation of g-C_3N_4 and Oxygen Doped g-C_3N_4 Catalysts

g-C_3N_4 was obtained by direct pyrolysis of melamine. Especially, 10 g melamine was put into an alumina crucible with a cover, then heated to 550 °C at a heating rate of 10 °C/min and kept at this temperature for 2 h in air atmosphere. The yield of g-C_3N_4 was about 35.8%.

The prepared g-C_3N_4 samples were further used to prepare oxygen doped g-C_3N_4 (O-g-C_3N_4). Typically, 1.0 g of g-C_3N_4 samples were added in 25 mL ultrapure water and were dispersed through ultrasonic treatment for 5 min. Then PMS solid was poured, and further treated at 60 °C for 30 min with ultrasonic power of 80 W. The product was collected by centrifugation, washing with ultrapure water, and then drying. The addition amount of PMS was 1, 2 ad 5 g. Accordingly, the resulted product was named as O-g-C_3N_4-1, O-g-C_3N_4-2 and O-g-C_3N_4-5.

3.3. Characterization

The morphology of samples was obtained by Hitachi SU8010 field emission SEM (Tokyo, Japan) and further confirmed by TEM (Tecnai G2 20 S-TWIN, Hillsboro, OR, USA). XRD was collected on a Bruker D8 Advance with Cu Kα radiation. XPS was analyzed on an AXIS-ULTRA DLD-600W instrument of Shimadzu (Shimadzu, Kyoto, Japan). The BET specific surface areas were obtained on an Autosorb iQ2 apparatus of Quantachrome (Anton Paar, Graz, The Republic of Austria). UV-vis DRS was collected on Shimadzu UV-2600 spectrometer (Shimadzu, Kyoto, Japan).

3.4. Photocatalytic Reaction

RhB was chosen as a model pollutant to compare the photocatalytic performance of g-C_3N_4 and O-g-C_3N_4. Typically, 50 mg catalysts mixed with 50 mL of RhB aqueous solution to obtain the catalyst load of 1 g/L and RhB concentration of 15 mol/L. pH of the reaction solution was not adjusted. The initial pH was about five and little changed during the reaction process. After stirring in the dark for 30 min at 300 rpm to reach the adsorption/desorption equilibrium between RhB and O-g-C_3N_4

catalysts, the reaction was processed by irradiation by a 500 W halogen lamp with cut-off filter ($\lambda >$ 420 nm) [49]. The lamp was placed in the middle of the reactor. A jacket out of the reactor filled with flowing water was used to keep the temperature of the system at 25 °C. The lamp was about 15 cm away from the suspension surface. During the reaction process, 1.5 mL solution was sampled and analyzed by eVolution 201 UV-visible spectrometer (Thermo Scientific, Waltham, MA, USA).

Pseudo first order reaction kinetics of $\ln(c/c_0) = -kt$ was used to fit RhB degradation in the photocatalytic g-C_3N_4 and O-g-C_3N_4.

3.5. Chemical Analysis

The concentrations of RhB and rhodamine 110 were analyzed with the UltiMate 3000 series HPLC (Thermo Scientific, Waltham, MA, USA). The other intermediates for RhB degradation by photocatalytic O-g-C_3N_4 were identified by LC-MS (1100 LC/MSD Trap, Agilent, CA, USA). The generated radicals were identified by electron spin resonance (ESR) assay.

4. Conclusions

In the paper, a facile method was developed to prepare oxygen doped g-C_3N_4 nanosheets by oxidation by peroxymonosulfate under ultrasonic treatment. Oxidation of g-C_3N_4 by PMS increased oxygen content from 1.8% for g-C_3N_4 to 6.9% for O-g-C_3N_4 nanosheets. The doping of oxygen-enhanced photocatalytic performance of O-g-C_3N_4 for activation of molecular oxygen, due to extended absorption to visible light and obviously improved separation of photo-generated charge carriers compared with g-C_3N_4 nanosheets. Superoxide radicals were identified as the main free radical for step by step N-deethylation reaction of rhodamine B (RhB) by O-g-C_3N_4 photocatalysis with the highest selectivity for rhodamine 110 of 75%. The degradation pathway of RhB by O-g-C_3N_4 photocatalysis is quite different from the non-selective decomposition of the chromophore in RhB by other radicals, such as hydroxyl radicals reported previously. This study, thus, provides a highly efficient g-C_3N_4 based photocatalyst for the activation of molecular oxygen for the green oxidation of organic pollutants.

Supplementary Materials: The following are available online at http://www.mdpi.com/2073-4344/10/1/6/s1, Figure S1: EDS and elemental composition of O-g-C_3N_4, Figure S2: EDS and elemental composition of g-C_3N_4, Figure S3: Photos of g-C_3N_4 and O-g-C_3N_4, Figure S4: RhB adsorption on surface of g-C_3N_4 and O-g-C_3N_4, Figure S5: Zeta potential of g-C_3N_4 and O-g-C_3N_4, Figure S6: Model for adsorption and stepwise N-deethylation process of RhB on O-g-C3N4 surface under visible light irradiation, Table S1: Comparison on the doped g-C_3N_4 for RhB degradation.

Author Contributions: Conceptualization, J.H.; methodology, G.N.; formal analysis, J.H.; Writing-Original Draft preparation, J.H.; Revision and Supervision Y.D. All authors have read and agreed to the published version of the manuscript.

Funding: This work was supported by the Fundamental Research Funds for the Central Universities (Grant No. CZT19005) and the Natural Science Foundation of Hubei Province of China (Grant No. 2018CFB623). We also appreciate the financial supports from the National Student Innovation Training Program (GCX1935).

Conflicts of Interest: The authors declare no conflict of interest.

References

1. Konstantinou, I.K.; Albanis, T.A. TiO_2-assisted photocatalytic degradation of azo dyes in aqueous solution: Kinetic and mechanistic investigations: A review. *Appl. Catal. B Environ.* **2004**, *49*, 1–14. [CrossRef]
2. Ruggieri, F.; Di Camillo, D.; Maccarone, L.; Santucci, S.; Lozzi, L. Electrospun Cu-, W- and Fe-doped TiO_2 nanofibres for photocatalytic degradation of rhodamine 6G. *J. Nanoparticle Res.* **2013**, *15*, 1982–1992. [CrossRef]
3. Cao, J.; Nie, W.; Huang, L.; Ding, Y.; Lv, K.; Tang, H. Photocatalytic activation of sulfite by nitrogen vacancy modified graphitic carbon nitride for efficient degradation of carbamazepine. *Appl. Catal. B Environ.* **2019**, *241*, 18–27. [CrossRef]

4. Cheng, J.; Hu, Z.; Li, Q.; Li, X.; Fang, S.; Wu, X.; Li, M.; Ding, Y.; Liu, B.; Yang, C. Fabrication of high photoreactive carbon nitride nanosheets by polymerization of amidinourea for hydrogen production. *Appl. Catal. B Environ.* **2019**, *245*, 197–206. [CrossRef]
5. Cheng, J.; Hu, Z.; Lv, K.; Wu, X.; Li, Q.; Li, Y.; Li, X.; Sun, J. Drastic promoting the visible photoreactivity of layered carbon nitride by polymerization of dicyandiamide at high pressure. *Appl. Catal. B Environ.* **2018**, *232*, 330–339. [CrossRef]
6. Mamba, G.; Mishra, A. Graphitic carbon nitride (g-C_3N_4) nanocomposites: A new and exciting generation of visible light driven photocatalysts for environmental pollution remediation. *Appl. Catal. B Environ.* **2016**, *198*, 347–377. [CrossRef]
7. Wang, H.; Jiang, S.; Chen, S.; Li, D.; Zhang, X.; Shao, W.; Sun, X.; Xie, J.; Zhao, Z.; Zhang, Q.; et al. Enhanced Singlet Oxygen Generation in Oxidized Graphitic Carbon Nitride for Organic Synthesis. *Adv. Mater.* **2016**, *28*, 6940–6945. [CrossRef] [PubMed]
8. Xu, S.; Zhou, P.; Zhang, Z.; Yang, C.; Zhang, B.; Deng, K.; Bottle, S.; Zhu, H. Selective oxidation of 5-hydroxymethylfurfural to 2, 5-furandicarboxylic acid using O_2 and a photocatalyst of Co-thioporphyrazine bonded to g-C_3N_4. *J. Am. Chem. Soc.* **2017**, *139*, 14775–14782. [CrossRef] [PubMed]
9. Zheng, Y.; Jiao, Y.; Chen, J.; Liu, J.; Liang, J.; Du, A.; Zhang, W.; Zhu, Z.; Smith, S.C.; Jaroniec, M. Nanoporous graphitic-C_3N_4@carbon metal-free electrocatalysts for highly efficient oxygen reduction. *J. Am. Chem. Soc.* **2011**, *133*, 20116–20119. [CrossRef] [PubMed]
10. Li, J.; Shen, B.; Hong, Z.; Lin, B.; Gao, B.; Chen, Y. A facile approach to synthesize novel oxygen-doped g-C_3N_4 with superior visible-light photoreactivity. *Chem. Commun.* **2012**, *48*, 12017–12019. [CrossRef]
11. Zhu, Y.-P.; Ren, T.-Z.; Yuan, Z.-Y. Mesoporous phosphorus-doped g-C_3N_4 nanostructured flowers with superior photocatalytic hydrogen eVolution performance. *ACS Appl. Mater. Interfaces* **2015**, *7*, 16850–16856. [CrossRef] [PubMed]
12. Wang, K.; Li, Q.; Liu, B.; Cheng, B.; Ho, W.; Yu, J. Sulfur-doped g-C_3N_4 with enhanced photocatalytic CO_2-reduction performance. *Appl. Catal. B Environ.* **2015**, *176*, 44–52. [CrossRef]
13. Sagara, N.; Kamimura, S.; Tsubota, T.; Ohno, T. Photoelectrochemical CO_2 reduction by a p-type boron-doped g-C_3N_4 electrode under visible light. *Appl. Catal. B Environ.* **2016**, *192*, 193–198. [CrossRef]
14. Cao, J.; Pan, C.; Ding, Y.; Li, W.; Lv, K.; Tang, H. Constructing nitrogen vacancy introduced g-C_3N_4 pn homojunction for enhanced photocatalytic activity. *J. Environ. Chem. Eng.* **2019**, *7*, 102984. [CrossRef]
15. Wang, Z.; Huang, Y.; Chen, M.; Shi, X.; Zhang, Y.; Cao, J.; Ho, W.; Lee, S.C. Roles of N-Vacancies over Porous g-C_3N_4 Microtubes during Photocatalytic NO_x Removal. *ACS Appl. Mater. Interfaces* **2019**, *11*, 10651–10662. [CrossRef] [PubMed]
16. Gao, J.; Wang, Y.; Zhou, S.; Lin, W.; Kong, Y. A facile one-step synthesis of Fe-doped g-C_3N_4 nanosheets and their improved visible-light photocatalytic performance. *ChemCatChem* **2017**, *9*, 1708–1715. [CrossRef]
17. Le, S.; Jiang, T.; Zhao, Q.; Liu, X.; Li, Y.; Fang, B.; Gong, M. Cu-doped mesoporous graphitic carbon nitride for enhanced visible-light driven photocatalysis. *RSC Adv.* **2016**, *6*, 38811–38819. [CrossRef]
18. Shi, A.; Li, H.; Yin, S.; Liu, B.; Zhang, J.; Wang, Y. Effect of conjugation degree and delocalized π-system on the photocatalytic activity of single layer g-C_3N_4. *Appl. Catal. B Environ.* **2017**, *218*, 137–146. [CrossRef]
19. Ma, S.; Zhan, S.; Jia, Y.; Shi, Q.; Zhou, Q. Enhanced disinfection application of Ag-modified g-C_3N_4 composite under visible light. *Appl. Catal. B Environ.* **2016**, *186*, 77–87. [CrossRef]
20. Hao, R.; Wang, G.; Tang, H.; Sun, L.; Xu, C.; Han, D. Template-free preparation of macro/mesoporous g-C_3N_4/TiO_2 heterojunction photocatalysts with enhanced visible light photocatalytic activity. *Appl. Catal. B Environ.* **2016**, *187*, 47–58. [CrossRef]
21. Sun, Q.; Lv, K.; Zhang, Z.; Li, M.; Li, B. Effect of contact interface between TiO_2 and g-C_3N_4 on the photoreactivity of g-C_3N_4/TiO_2 photocatalyst: (0 0 1) vs (1 0 1) facets of TiO_2. *Appl. Catal. B Environ.* **2015**, *164*, 420–427.
22. Cui, L.; Ding, X.; Wang, Y.; Shi, H.; Huang, L.; Zuo, Y.; Kang, S. Facile preparation of Z-scheme WO_3/g-C_3N_4 composite photocatalyst with enhanced photocatalytic performance under visible light. *Appl. Surf. Sci.* **2017**, *391*, 202–210. [CrossRef]
23. Ye, L.; Liu, J.; Jiang, Z.; Peng, T.; Zan, L. Facets coupling of BiOBr-g-C_3N_4 composite photocatalyst for enhanced visible-light-driven photocatalytic activity. *Appl. Catal. B Environ.* **2013**, *142*, 1–7. [CrossRef]
24. He, Y.; Zhang, L.; Teng, B.; Fan, M. New application of Z-scheme Ag_3PO_4/g-C_3N_4 composite in converting CO_2 to fuel. *Environ. Sci. Technol.* **2014**, *49*, 649–656. [CrossRef] [PubMed]

25. Guo, S.; Zhu, Y.; Yan, Y.; Min, Y.; Fan, J.; Xu, Q. Holey structured graphitic carbon nitride thin sheets with edge oxygen doping via photo-Fenton reaction with enhanced photocatalytic activity. *Appl. Catal. B Environ.* **2016**, *185*, 315–321. [CrossRef]
26. Fu, J.; Zhu, B.; Jiang, C.; Cheng, B.; You, W.; Yu, J. Hierarchical Porous O-Doped g-C_3N_4 with Enhanced Photocatalytic CO_2 Reduction Activity. *Small* **2017**, *13*, 1603938. [CrossRef]
27. Zeng, Y.; Liu, X.; Liu, C.; Wang, L.; Xia, Y.; Zhang, S.; Luo, S.; Pei, Y. Scalable one-step production of porous oxygen-doped g-C_3N_4 nanorods with effective electron separation for excellent visible-light photocatalytic activity. *Appl. Catal. B Environ.* **2018**, *224*, 1–9. [CrossRef]
28. Huang, Y.H.; Huang, Y.F.; Huang, C.I.; Chen, C.Y. Efficient decolorization of azo dye Reactive Black B involving aromatic fragment degradation in buffered Co^{2+}/PMS oxidative processes with a ppb level dosage of Co^{2+}-catalyst. *J. Hazard. Mater.* **2009**, *170*, 1110–1118. [CrossRef]
29. Yang, S.; Wang, P.; Yang, X.; Shan, L.; Zhang, W.; Shao, X.; Niu, R. Degradation efficiencies of azo dye Acid Orange 7 by the interaction of heat, UV and anions with common oxidants: Persulfate, peroxymonosulfate and hydrogen peroxide. *J. Hazard. Mater.* **2010**, *179*, 552–558. [CrossRef]
30. Xu, J.; Zhang, L.; Shi, R.; Zhu, Y. Chemical exfoliation of graphitic carbon nitride for efficient heterogeneous photocatalysis. *J. Mater. Chem. A* **2013**, *1*, 14766–14772. [CrossRef]
31. Dong, F.; Li, Y.; Wang, Z.; Ho, W.K. Enhanced visible light photocatalytic activity and oxidation ability of porous graphene-like g-C_3N_4 nanosheets via thermal exfoliation. *Appl. Surf. Sci.* **2015**, *358*, 393–403. [CrossRef]
32. Zhou, S.; Liu, Y.; Li, J.; Wang, Y.; Jiang, G.; Zhao, Z.; Wang, D.; Duan, A.; Liu, J.; Wei, Y. Facile in situ synthesis of graphitic carbon nitride (g-C_3N_4)-N-TiO_2 heterojunction as an efficient photocatalyst for the selective photoreduction of CO2 to CO. *Appl. Catal. B Environ.* **2014**, *158–159*, 20–29. [CrossRef]
33. Yang, L.; Huang, J.; Shi, L.; Cao, L.; Yu, Q.; Jie, Y.; Fei, J.; Ouyang, H.; Ye, J. A surface modification resultant thermally oxidized porous g-C_3N_4 with enhanced photocatalytic hydrogen production. *Appl. Catal. B Environ.* **2017**, *204*, 335–345. [CrossRef]
34. Cao, S.-W.; Liu, X.-F.; Yuan, Y.-P.; Zhang, Z.-Y.; Liao, Y.-S.; Fang, J.; Loo, S.C.J.; Sum, T.C.; Xue, C. Solar-to-fuels conversion over In_2O_3/g-C_3N_4 hybrid photocatalysts. *Appl. Catal. B Environ.* **2014**, *147*, 940–946. [CrossRef]
35. Ye, L.; Chen, S. Fabrication and high visible-light-driven photocurrent response of g-C_3N_4 film: The role of thiourea. *Appl. Surf. Sci.* **2016**, *389*, 1076–1083. [CrossRef]
36. Yang, F.; Lublow, M.; Orthmann, S.; Merschjann, C.; Tyborski, T.; Rusu, M.; Kubala, S.; Thomas, A.; Arrigo, R.; Hävecker, M. Metal-Free Photocatalytic Graphitic Carbon Nitride on p-Type Chalcopyrite as a Composite Photocathode for Light-Induced Hydrogen eVolution. *ChemSusChem* **2012**, *5*, 1227–1232. [CrossRef]
37. Du, X.; Yi, X.; Wang, P.; Deng, J.; Wang, C.-C. Enhanced photocatalytic Cr(VI) reduction and diclofenac sodium degradation under simulated sunlight irradiation over MIL-100(Fe)/g-C_3N_4 heterojunctions. *Chin. J. Catal.* **2019**, *40*, 70–79. [CrossRef]
38. Li, X.; Liu, C.; Wu, D.; Li, J.; Huo, P.; Wang, H. Improved charge transfer by size-dependent plasmonic Au on C_3N_4 for efficient photocatalytic oxidation of RhB and CO_2 reduction. *Chin. J. Catal.* **2019**, *40*, 928–939. [CrossRef]
39. Barras, A.; Cordier, S.; Boukherroub, R. Fast photocatalytic degradation of rhodamine B over $[Mo_6Br_8(N_3)_6]^{2-}$ cluster units under sun light irradiation. *Appl. Catal. B Environ.* **2012**, *123–124*, 1–8. [CrossRef]
40. Hu, X.; Mohamood, T.; Ma, W.; Chen, C.; Zhao, J. Oxidative decomposition of rhodamine B dye in the presence of VO_2^+ and/or Pt (IV) under visible light irradiation: N-deethylation, chromophore cleavage, and mineralization. *J. Phys. Chem. B* **2006**, *110*, 26012–26018. [CrossRef]
41. Li, W.; Li, D.; Meng, S.; Chen, W.; Fu, X.; Shao, Y. Novel Approach To Enhance Photosensitized Degradation of Rhodamine B under Visible Light Irradiation by the $Zn_xCd_{1-x}S/TiO_2$ Nanocomposites. *Environ. Sci. Technol.* **2011**, *45*, 2987–2993. [CrossRef] [PubMed]
42. Murcia López, S.; Hidalgo, M.C.; Navío, J.A.; Colón, G. Novel Bi_2WO_6–TiO_2 heterostructures for Rhodamine B degradation under sunlike irradiation. *J. Hazard. Mater.* **2011**, *185*, 1425–1434. [CrossRef] [PubMed]
43. Chen, F.; Zhao, J.; Hidaka, H. Highly selective deethylation of rhodamine B: Adsorption and photooxidation pathways of the dye on the TiO_2/SiO_2 composite photocatalyst. *Int. J. Photoenergy* **2003**, 5.
44. Fu, H.; Zhang, S.; Xu, T.; Zhu, Y.; Chen, J. Photocatalytic Degradation of RhB by Fluorinated Bi_2WO_6 and Distributions of the Intermediate Products. *Environ. Sci. Technol.* **2008**, *42*, 2085–2091. [CrossRef] [PubMed]

45. Watanabe, T.; Takizawa, T.; Honda, K. Photocatalysis through excitation of adsorbates. 1. Highly efficient N-deethylation of rhodamine B adsorbed to cadmium sulfide. *J. Phys. Chem.* **1977**, *81*, 1845–1851. [CrossRef]
46. Li, Z.; Yang, Q.; Chen, C.; Zhang, Z.; Fang, X. Enhanced photocatalytic performance of polymeric C_3N_4 doped with theobromine composed of an imidazole ring and a pyrimidine ring. *Chin. J. Catal.* **2019**, *40*, 875–885. [CrossRef]
47. Zhang, J.; Mao, X.; Xiao, W.; Zhuang, Y. Photocatalytic degradation of sulfamethazine by graphitic carbon nitride-modified zinc molybdate: Effects of synthesis method on performance, degradation kinetics, and mechanism. *Chin. J. Catal.* **2017**, *38*, 2009–2020. [CrossRef]
48. Wang, F.; Chen, P.; Feng, Y.; Xie, Z.; Liu, Y.; Su, Y.; Zhang, Q.; Wang, Y.; Yao, K.; Lv, W.; et al. Facile synthesis of N-doped carbon dots/g-C_3N_4 photocatalyst with enhanced visible-light photocatalytic activity for the degradation of indomethacin. *Appl. Catal. B Environ.* **2017**, *207*, 103–113. [CrossRef]
49. Qin, Y.; Ding, Y.; Tang, H. Highly efficient visible-light photocatalytic activity of graphitic carbon nitride prepared from melamine-thiourea molecular composite. *J. Environ. Chem. Eng.* **2016**, *4*, 4374–4384. [CrossRef]